Journal of Power Sources 467 (2020) 228360

Contents lists available at ScienceDirect

Journal of Power Sources

journal homepage: www.elsevier.com/locate/jpowsour

Generalized separator failure criteria for internal short circuit of lithium-ion battery

Chunhao Yuan [a,b], Lubing Wang [c,d], Sha Yin [c,d], Jun Xu [a,b,*]

[a] Department of Mechanical Engineering and Engineering Science, The University of North Carolina at Charlotte, Charlotte, NC, 28223, USA
[b] Vehicle Energy & Safety Laboratory (VESL), North Carolina Motorsports and Automotive Research Center, The University of North Carolina at Charlotte, Charlotte, NC, 28223, USA
[c] Department of Automotive Engineering, School of Transportation Science and Engineering, Beihang University, Beijing, 100191, China
[d] Vehicle Energy & Safety Laboratory (VESL), Beihang University, Beijing, 100191, China

HIGHLIGHTS

- Two representative short circuit modes are related to separator deformation status.
- A detailed computational model of anode-separator-cathode stack is established.
- A constitutive model of separator with mechanical anisotropy is developed.
- Universal separator failure criteria for short circuit are proposed and validated.

GRAPHICAL ABSTRACT

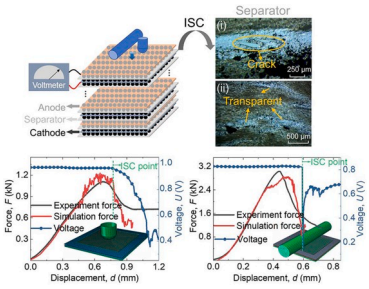

ARTICLE INFO

Keywords:
Lithium-ion battery
Separator
Internal short circuit criteria
Methodology

ABSTRACT

To enable the understanding of the internal short circuit mechanism triggered by separator failure, mechanical indentation loadings are designed to create the deformation of the separator in a precisely controllable way. Herein, two characteristic short-circuit types are observed in anode-separator-cathode stack upon mechanical abusive loading, i.e., rapid and gentle voltage drop. Through the ex-situ experiment, the rapid voltage drop is due to the direct contact between cathode and anode as a result of separator fracture, while the gentle voltage drop is related to the flattening of the separator with the absence of its function to isolate electron transfer. The developed detailed numerical models, considering the failure of anode and cathode and the anisotropy of separator, can well describe the mechanical responses of components and stack. Thanks to the numerical computation model and computation, we establish and validate the generalized short-circuit criteria for the two representative failure modes based on the volumetric strain and equivalent strain of separator. Results provide a powerful and generalized tool aiming for the design of next-generation separator technology, enabling a more fundamental and effective way for future ISC detection, monitoring, and evaluation which can be embedded within the battery management system.

* Corresponding author. Department of Mechanical Engineering and Engineering Science, The University of North Carolina at Charlotte, Charlotte, NC, 28223, USA.
E-mail address: jun.xu@uncc.edu (J. Xu).

https://doi.org/10.1016/j.jpowsour.2020.228360
Received 1 April 2020; Received in revised form 1 May 2020; Accepted 13 May 2020
Available online 27 May 2020
0378-7753/© 2020 Elsevier B.V. All rights reserved.

1. Introduction

With the increasingly wide application of lithium-ion batteries (LIBs) in electric vehicles, large energy storage facilities, as well as 3C products (i.e., computers, cellphones and communication devices) [1,2], safety issues associated with LIBs, become more and more noteworthy since many of the incidents are catastrophic [3]. The first safety-related milestone event should be the short circuit of batteries [4]. Particularly, once an internal short circuit (ISC) is triggered, the generated Ohmic heat inside LIBs may activate the exothermic (electro) chemical reactions, which may lead to thermal runaway, or sometimes even fires or explosions [4–7].

ISC can be triggered by internal causations such as puncturation from lithium dendrite growths [8] and broken particle penetration [9,10], as well as various sorts of external abusive scenarios, such as mechanical [7,11–13], electrical [14] and thermal [15] abusive cases. No matter how ISC is triggered, the fundamental physical reason is the occurrence of electron transfer between cathodes and anodes. Sandwiched between the cathode and anode, the separator is the only component that functions to allow the free movements of ions while blocking the electron transfer [16]. Therefore, the failure of separator integrity is the direct cause of ISC, and the structure-performance relation of separator determines LIB safety [17].

Plenty of pioneering research efforts have been endeavored to understand the properties of the separator, e.g., porosity [18–20], wettability [18,19], shrinkage [18,19], thermal behavior [18–22] and mechanical property [23–27]. Electrochemical/chemical stability and mechanical robustness are required for the separator to accommodate to its working environment [20,23]. Various experiments and models were designed and established to characterize the mechanical properties of the separator. Due to the microstructure of the material and polymer nature, the separator showed obvious anisotropic, viscoelastic properties, and strain rate dependency [24,25,28,29]. Experiments showed that mechanical stress or deformation of the separator could lead to impedance increase and capacity fade in battery [30,31]. Electrolyte solvents can also influence the mechanical properties of the separator, e.g., swelling and softening [32,33]. Viscoelastic constitutive model [23,34], homogenized finite element (FE) model considering anisotropic properties [26,35], 2D and 3D microstructural FE models from stochastic reconstruction used to describe the anisotropic responses of separator [36,37] were developed to further explore properties of the separator. On the other hand, considering the mechanical integrity requirement, the mechanical failure of the separator was also explored. Separators fabricated by different compositions and fabrications showed different failure modes under uniaxial tensile loading [24,26]. Through interrupted tensile tests, the deformation and failure mechanisms of separator under tension in different directions were illustrated [38]. The mechanical strength of separator suffered degradation during charge-discharge cycling [39]. Under biaxial tension, the first principal strains at failure point for Celgard 2325 and Celgard 2075 measured by DIC were found to be about 0.34 and 0.43, respectively [40].

However, few studies focus on the relation of mechanical properties of separators with the electrochemical performance of LIBs. The challenge stems from the difficulties in disassembling the battery on/after ISC, and generally, the separator would be melted in a very short time after ISC. By biaxial punch tests, different failure modes of the separator, i.e., thinning or crack, were hypothesized to cause the soft and hard short circuits [41], which is not validated yet and needs further study. Progressive indentation tests on large-format pouch cells indicated that thinning of the separator may result in ISC [42]. With the separator modeled as an open-cell foam, its ionic conductivity can be derived in terms of stress. Thus its mechanical status is implicitly related to the electrochemical behavior of LIBs [43]. Also, the mechanical properties of the separator can be characterized through a stack of anode-separator-cathode, but no connection was bridged between the mechanical behavior of the separator and ISC [44]. The quantitative relation between ISC point and the mechanical status of the separator is in urgently need of full investigation under the condition when battery electrochemical performance is directly related to the mechanical behavior of separator.

To unravel the fundamental behavior of the separator leading to ISC, first of all, this paper designed a series of experiments by using the anode-separator-cathode stack as testing samples to mimic the working environment for the separator. To quantitatively characterize the deformation status of the separator at ISC point, a detailed FE model is then established and verified. The constitutive models of detailed battery components are developed through out-of-plane compression and in-plane tension tests. Finally, ISC criteria are developed based on the mechanical status of the separator and further validated by flat-head indentation.

2. Experimental

2.1. Anode-separator-cathode stack experiment

There are three major reasons that we study the layered stack instead of the entire cell. First of all, In the commercial pouch cell where all component layers are sealed, once the ISC is triggered, there will be much heat generated inside the battery, such as Joule heat, side-reaction heat, which may cause thermal runaway or even fires [2]. Under such a high temperature, the separator will melt, and it's difficult for us to analyze the relation of mechanical properties and electrochemical performance without the exclusion of thermal effects. If sealed in pouch material, the short circuit position inside the battery cell is also unknown since there are several layers of cathode and anode, while the short circuit position is clear in stack experiment of this study (i.e., the loading area). Secondly, the sealed pouch battery cell will be disassembled after mechanical loading to investigate the mechanical state of the separator, during which the separator may suffer from extra damage. Last but not least, we'd like to have the results in a more generalized and fundamental without any constrains to the battery type (e.g., cylindrical battery, prismatic battery, pouch cell, etc.).

To mimic the battery inside structures to the largest extent and eliminate the possible heat influence over the separator, anode, separator, and cathode samples prepared in square shape were stacked. By considering the experiment feasibility and efficiency, a representative unit of five stacks in the anode-separator-cathode-separator sequence was chosen. The sizes of the square sample for cathode, anode, and separator were 30*30 mm^2, 30*30 mm^2 and 40*40 mm^2, respectively. A larger separator guaranteed the full coverage of cathode and anode during loading. The cathode and anode used in the study were disassembled from commercially available cylindrical 18650 NCA/graphite battery which was previously discharged to its cut-off voltage (i.e., 0% SOC), and their thicknesses were 0.17 mm, 0.2 mm, respectively. The central angle for the electrode sample is about 190° (Fig. S1). With such a wide angle in geometry and the free boundary conditions for the assembled electrode samples, the effect of residual stress is negligible. The integrity of each electrode stack was checked to guarantee the reliability of the experiment. The area of electrodes in the upper electrode pair is 30*40 mm^2, whose active material on the edge was removed, and a piece of metal was clamped with the current collectors (Fig. 1(a)) to measure the voltage. The assembly was covered with insulating tape to avoid the contact of cathode and anode through the compression platen. During the preparation of the anode-separator-cathode-separator stacks, each layer was piled in a layer-on-layer way, such that the electrodes were placed at the center of separators. Based on these operations, electrodes were overlapped and insulated by separators, and the physical contact of cathode and anode was guaranteed to be isolated. The commercial Celgard 2500 single-layer polypropylene separator with a thickness of 25 μm was chosen. The stack was then immersed into electrolyte $LiPF_6$ (detailed information in Table S1), and the same electrolyte about 1 ml was splashed to the separator of the

stack before the experiment to improve ion conduction between electrodes (see Table S2). To minimize the effect of exposure to the air, the time gap was very short from disassembling the battery cell to preparing the final samples and performing the experiment. However, the electrolyte still inevitably evaporated and the electrolyte concentration was still lower than that of commercial LIBs, such that the voltage measured was about 0.75 V, much lower than 3 V. Considering the evaporation of the electrolyte and its harm to experimenters, during the experiment, we wore the industrial gas masks, experimental goggles, lab coats, and gloves to block harmful gases and avoid skins exposed in the air. In addition, the ventilation in the lab was always working during the entire experiment process, even long after the experiment to exhaust harmful substances.

A small pre-compression force of 10 N was applied for the stack to gain a uniform contact among cathode, anode, and separator. After the pre-compression, adhesive tapes were used to fix the edge of the stack to keep the uniform contact between these stack layers. To efficiently and controllably trigger the ISC, and mimic all possible mechanical deformation scenarios, the mechanical abusive loading is adopted here. Two typical mechanical loading types were selected, i.e., sphere indentation (Fig. 1(b)) and cylinder compression (Fig. 1(c)). The indentor diameters for the sphere and cylinder were 12 mm and 10 mm, respectively. The loading velocity was 1 mm/min to ensure that no strain rate effect was involved. Since the upper anode-separator-cathode pair near the indentor would suffer much more severe damage than the lower counterparts [45], it would be easier to focus on the electrochemical response of the upper electrode pair which means that only the voltage of the upper electrode pair was measured by Agilent 34410 with a frequency of 20 Hz. Consequently, the lower electrode pairs were considered as the bearing substrate. As such, short-circuit behavior discussed in the following refers to the upper electrode pair. To ensure the reliability of the voltage measurement and to guarantee the close contact of anode-separator-cathode, the pre-loading of 20 N was applied onto the indentor before the experiment.

As Fig. 1(d) and (e) show, for sphere indentation, the reaction force increases with loading displacement d until reaching the maximum force about 1.1 kN at the displacement 0.67 mm, then the force gradually drops. Voltage starts to decrease gently after the onset of the force drop, which implies separator gradually loses its function of blocking electron transfer. While for cylinder loading, the force decreases at the displacement of about 0.45 mm with maximum force about 3 kN. Moreover, the voltage drops abruptly which is quite different from sphere indentation and may be caused by direct contact between electrodes, and the voltage recovery may be caused by the melt of the current collector [4]. To avoid the edge effect of the exposed current collector (due to the removing of active materials), the axis of cylindrical indentor was set along the short side (i.e. 30 mm) of the electrode. Active material within the loading area would inevitably be peeled off during the severe mechanical loadings, but the bare current collectors still cannot contact the other electrode due to the isolation of the larger size separator. Therefore, it is safe to conclude that the damage of separator within loading area rather than the direct contact of current collectors should be the responsible reason for the abrupt voltage drop during compression. The voltage drop occurs after the peak force which implies the electrodes come to damage earlier than the failure of the separator. Also, one may observe excellent repeatability for force-displacement curves while the starting points of voltage drop are not the same due to the existing experimental differences. The difference in voltage drop rate in the two loading conditions may be caused by different stress states of battery components, i.e. compression in sphere indentation and shear in cylinder loading. Note that since the experiments were conducted in an open environment such that the electrolyte would inevitably evaporate leading to different initial voltage values. Such difference is trivial to our analysis since the voltage keeps constant before ISC and our focus is on ISC behavior.

Since two different internal short-circuit types, i.e., gradual and

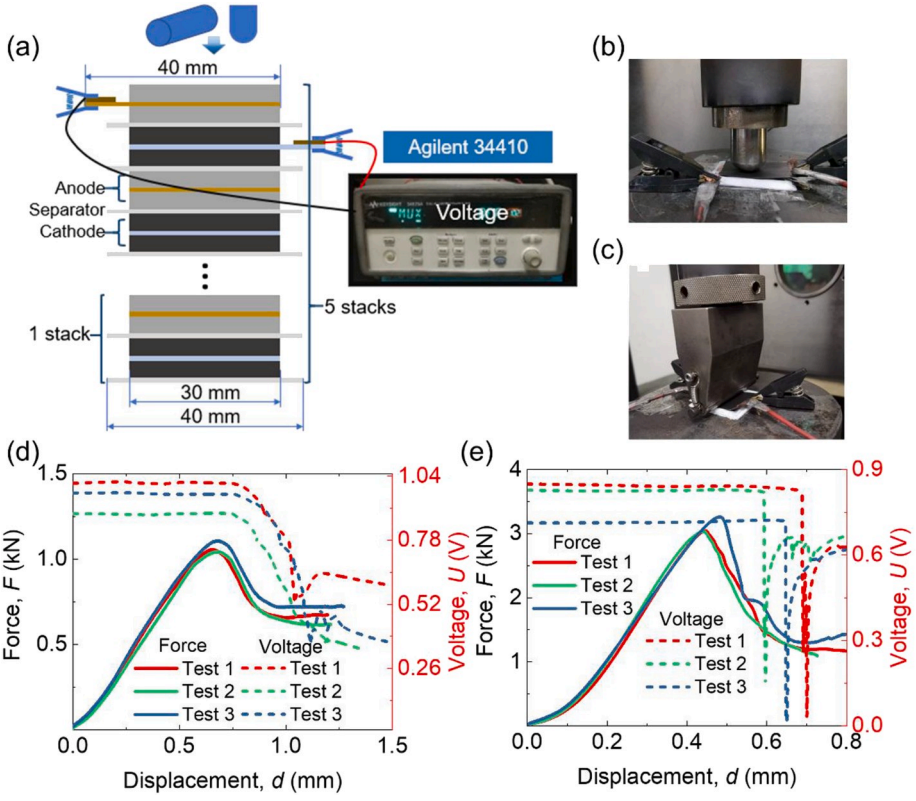

Fig. 1. (a) Schematic illustration of loading conditions. Schematic diagram of different loading types: (b) sphere indentation and (c) cylinder compression. Typical results of indentation experiments by (d) spherical indentor and (e) cylindrical indentor.

rapid voltage drops, were consistently observed from repeated experiments, ex-situ experiments were designed to unravel the status of the separator in these two scenarios. In practice, we stopped the loading once the voltage drop was captured, then the separator in the upper electrode pair was taken out for the observation of the morphology. For sphere indentation here, the voltage still decreases even if the loading was stopped, as shown in Fig. 2(a). Note that the stop point is always a bit lagging behind the ISC triggering point due to the manual operation delay. The industrial digital camera UCMOS05100KPA in Fig. 2(b) was used to observe the morphology of the separator. The observations in Fig. 2(c) demonstrate that the separator was transparent but free of any crack. This serves as direct evidence that the ISC can be triggered without separator fracture. Due to the Poisson's effect, the thinning of the separator in the thickness direction will be accompanied by the stretching in the in-plane direction, such that the results caused by compression can be equivalent to that by tension mechanically, as shown in Fig. S3. Considering the fact that the Poisson ratio of polypropylene (PP) is about 0.42 [46], we infer the in-plane dilation of the separator should be large (since the Poisson's effect is obvious). Furthermore, from the previous study [38], the SEM images of PP separator under TD tension at different strains show that the pores become larger and rounder with the strain [38]. Then we can infer that the pore size of the separator under sphere loading increases with the loading. Under this circumstance, the size of the micropore within

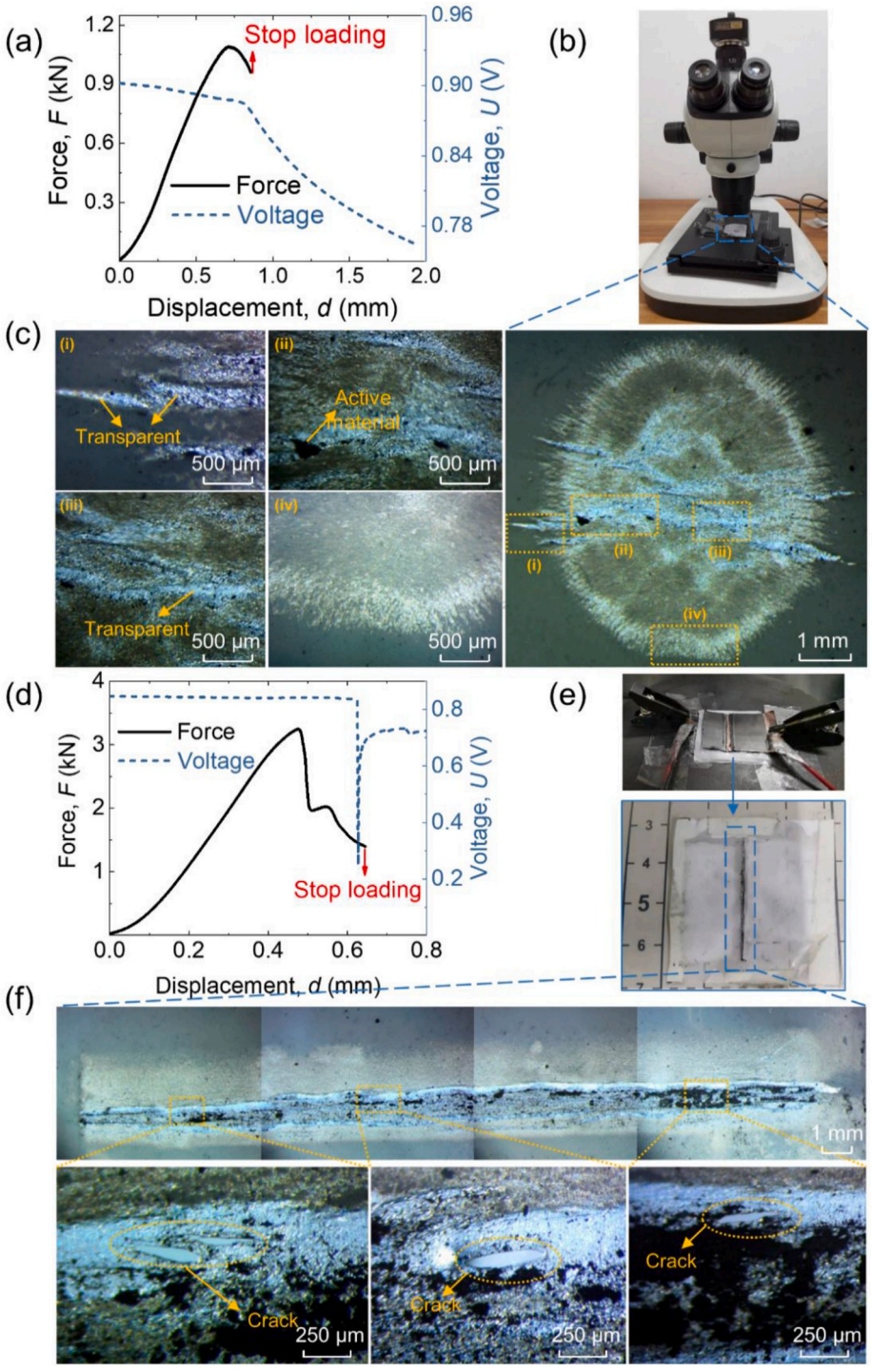

Fig. 2. Micro-morphology of the separator at the loading-stop point when ISC is triggered. Sphere indentation: (a) force/voltage-displacement curves, (b) microscope UCMOS05100KPA with the resolution of 1280*960, (c) the separators is flattening and transparent without any cracks. Note that the black area is the result of active materials left on the separator. Cylinder compression: (d) force/voltage-displacement curves, (e) separator taken out from the anode-separator-cathode stack, (f) micro-morphology of the separator with cracks surrounding.

separator increased due to the flattening of the separator sheet such that electron transferring is no longer blocked so that ISC occurs (i.e., the separator "dysfunctions"). The active material particles of cathode and anode may contact each other when the pore size increases. The contact resistance of active materials was proven to be much larger than that of current collectors [4], which can explain the gradual decrease of voltage. From the physical point of view, the voltage drop is directly related to the internal current flowing between cathode and anode which is resulted from the electron transfer. Thus the voltage drop is related to the functional integrity of the separator. From Fig. 1(d), we can infer that the voltage decreases gradually which is caused by that the separator gradually loses its function to block the electron transferring capability.

For cylinder compression, we also stopped the loading once ISC was triggered, as shown in Fig. 2(d), while several cracks were observed within the vicinity of the loading area of separator in Fig. 2(f). In this condition, the separator was mechanical damaged (or fractured), which leads to the direct contact between cathode and anode, causing a sharp voltage drop. As for the cylinder compression, the anode-separator-cathode stack bears shear force [47]. Subject to considerable shear stress, the process of separator becoming transparent is very short, immediately followed by the cracking of separator, which can explain the stable voltage before the short circuit.

Therefore, the flattening of the separator without any cracks to a certain extent leads to a "gentle ISC" such that voltage drops mildly while the fracture of the separator is responsible for a "sharp ISC" with rapid voltage drop. This serves as a first direct step to correlate separator morphology with ISC in a qualitative manner. Since similar internal short circuit behaviors can also be observed in other types of separators, e.g., three-layer separator [41], for simplicity, we only choose single-layer separators here to develop our methodology.

2.2. Mechanical behavior characterization of the separator

Further characterization of the separator lays a foundation for the following FE model. As such, various experiments were designed, including through-thickness compression, in-plane tension of machine direction (MD), diagonal direction (DD) and transverse direction (TD).

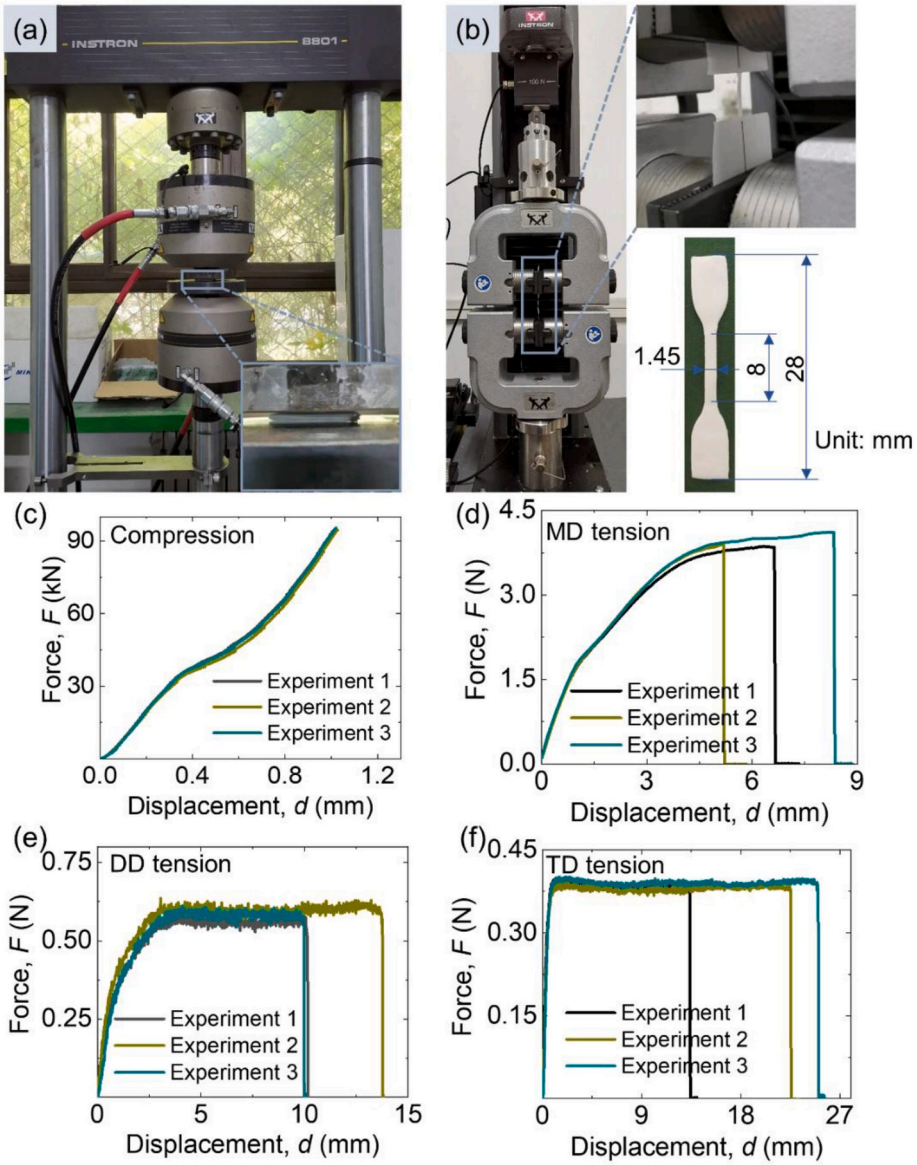

Fig. 3. Compression and tension experiments for the separator. Schematics of experimental setups for: (a) out-of-plane compression test (INSTRON 8801, 1 mm/min) and (b) in-plane tension test (INSTRON 2345, 10 mm/min) and sample size in tension test. Force-displacement responses of the separator under different loading conditions: (c) compression, (d) MD tension, (e) DD tension and (f) TD tension; 3 repeated test were recorded for each loading condition to show the consistency.

The compression experiment was performed based on INSTRON 8801 with a maximum loading capacity of 100 kN, as depicted in Fig. 3(a), at the loading velocity of 1 mm/min. The compression sample was prepared by stacking of 40 layers of separators, where separators were tailored into a square shape with a 40 mm edge length. The tension experiment was taken by INSTRON 2345 with a maximum capacity of 100 N (Fig. 3(b)). The tension separator was cut into a dog-bone shape [23], whose detailed size information is indicated in Fig. 3(b). The tension velocity was selected as 10 mm/min so that the strain rate of separator in the tension test is approximately the same to that in the compression test, i.e., about 0.015 s^{-1}.

The experiment results of compression and tension are summarized in Fig. 3(c)–(f). Three repeated test results are plotted for each loading condition, and the results show great consistency. According to the force-displacement responses in different directions, the sample shows obvious anisotropic properties. The force-displacement curve of the compression test shows a linear stage followed by a nonlinear enhancement. For in-plane tension, MD tension shows the maximum tensile strength with the minimum failure strain, while the weakest tensile strength occurs in TD tension, which is mainly attributed to the microstructure and pre-stretching during the manufacturing process of the separator [24]. Moreover, the electrolyte was splashed onto the separator to investigate the influence of electrolyte on the properties of the separator, and the results show the electrolyte effect is negligible in the interested loading conditions in this study (see Fig. S4).

3. Numerical modeling

To quantitatively characterize the mechanical deformation of the separator during the sphere indentation and cylinder compression, and to establish quantitative relationships between the separator deformation status and the onset of ISC, detailed numerical modeling is established to accurately describe the mechanical response for battery components (i.e., cathode, anode, and separator) and anode-separator-cathode stack. In this study, all the numerical modeling work is performed based on ABAQUS software platform.

3.1. Cathode and anode modeling

The samples of cathode and anode were disassembled from commercial cylindrical 18650 NCA/graphite batteries. The cathode and anode are assumed to be isotropic, whose force-displacement responses in through-thickness compression are taken from the previous study in our group [48]. The compression sample for the cathode is the stacking of 32-layer cathode plates in a square shape with 30 mm edge length, the same setup for anode compression sample. For simplicity and computational efficiency, such a 32-layer electrode is modeled by a "block" using C3D8R solid elements. The crushable foam material model is used to describe the porous structural properties of cathode and anode. Volumetric hardening is selected to describe the crushable foam plasticity model, and the compression/hydrostatic yield stress ratio is specified as 2.3/0.05. The input constitutive stress-strain curves for cathode and anode are obtained from their force-displacement responses in Fig. 4(a) and (b), respectively. The mechanical properties and section properties of cathode and anode are summarized in Table 1.

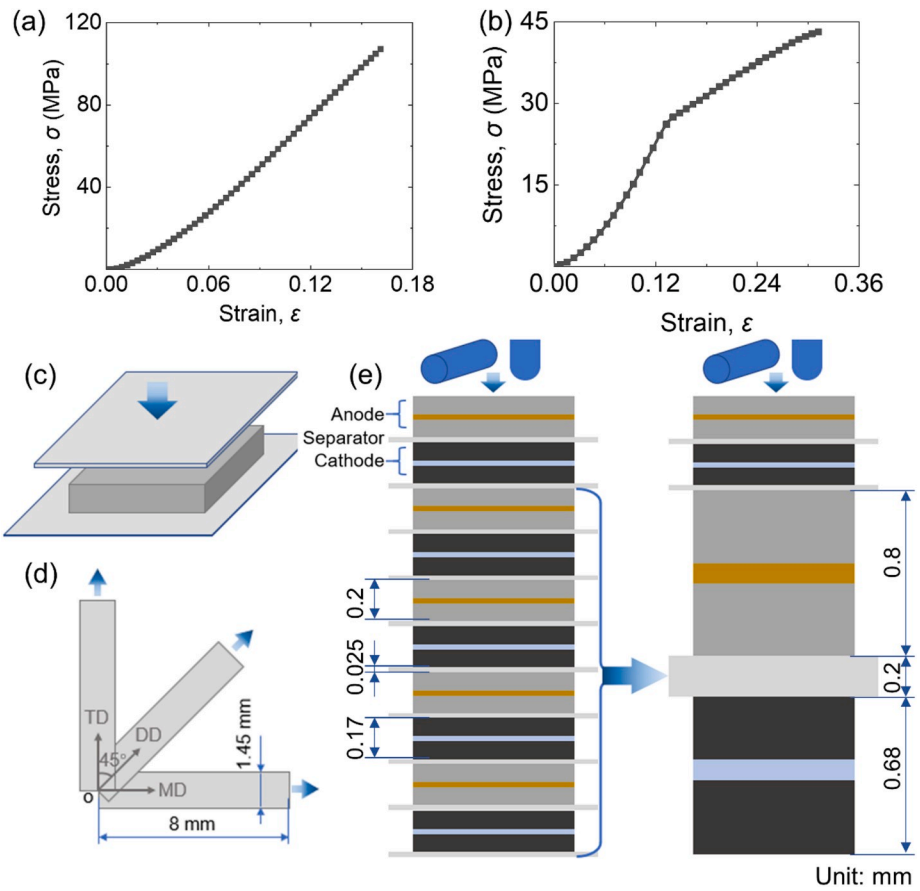

Fig. 4. Input constitutive stress-strain curves for (a) cathode and (b) anode. Schematic illustration of different models for the separator under (c) out-of-plane compression and (d) MD, DD, and TD tensions. (e) Equivalent modeling of the anode-separator-cathode stack model: the repeated anode-separator-cathode stack unit is replaced by a representative stack unit.

Table 1
Mechanical properties and section properties of components.

	Cathode	Anode	Separator
Material composition	Active material/Al	Active material/Cu	Single-layer PP
Density (kg/m^3)	7850	2270	1200
Thickness (mm)	0.17	0.2	0.025
Compression yield stress ratio	2.3	2.3	–
Hydrostatic yield stress ratio	0.05	0.05	–
Element type	Solid/C3D8R	Solid/C3D8R	Solid/C3D8R
Material type	Crushable foam	Crushable foam	User material by VUMAT

3.2. Separator modeling

Since separator shows obvious anisotropy, and there is no available material model in ABAQUS that can accurately describe such anisotropic properties, ABAQUS/Explicit subroutine VUMAT is adopted to define the anisotropic constitutive relationship for the separator. The details of the VUMAT can be referred to the Supplementary Material. The stress updating functions are listed as follows:

$$\sigma_{ii}^{new} = \sigma_{ii}^{old} + E_{ii}\Delta\varepsilon_{ii} \quad (i = 1, 2, 3) \tag{1}$$

$$\sigma_{ij}^{new} = \sigma_{ij}^{old} + 2G_{ij}\Delta\varepsilon_{ij} \quad (i \neq j, \quad i, j = 1, 2, 3) \tag{2}$$

where 1, 2, 3 represent TD, MD and through-thickness directions, respectively; σ_{ii}^{old} and σ_{ii}^{new} $(i = 1, 2, 3)$ represent normal stress before and after stress updating, respectively; σ_{ij}^{old} and $\sigma_{ij}^{new}(i \neq j, \quad i, j = 1, 2, 3)$ is shear stress before and after stress updating, respectively; E_{ii} $(i = 1, 2, 3)$ is Young's modulus in normal directions, G_{ij} $(i \neq j, \quad i, j = 1, 2, 3)$ is shear modulus; $\Delta\varepsilon_{ij}$ $(i, j = 1, 2, 3)$ represent strain increment in the corresponding directions.

For normal stresses updating, Young's moduli are assumed to vary with strain according to the stress-strain curves obtained from the force-displacement responses in experiments. For shear stresses updating, the shear moduli are assumed to be constant as 100 MPa [28] and G_{12} is assumed to be 20 MPa if $\varepsilon_{12} \geq 0.005$.

To validate the developed constitutive model for the separator, four typical loading conditions are considered, i.e., through-thickness compression, MD, DD, and TD tension. For the compression model, 40-layer separators are modeled by a block to reduce the computational cost while still maintain high confidentiality (Fig. 4(c)). For the tension model, only the focused rectangular area is taken into consideration since this area of the dog-bone sample is considered as a valid loading zone (Fig. 4(d)). The mechanical properties and section properties of the separator can be found in Table 1.

3.3. Anode-separator-cathode stack modeling

Based on the modeling work of component constitutive behavior, the anode-separator-cathode stack upon sphere indentation and cylinder compression is modeled. Since there are five stacks and only electrochemical behavior of the upper electrode pair is considered, the lower four repeated stacks are replaced with an equivalent representative electrode pair to improve computation efficiency, where cathode and anode are four-times thicker, and separator is eight-times thicker, as shown in Fig. 4(e). Moreover, since the ISC occurs during the force drop stage (i.e., mechanical failure stage) under both loading cases, then the failure of components should be taken into consideration. Because the cathode and anode mainly bear the loading and failure of the separator is related to ISC i.e. voltage drop, then the force drop is only attributed to the failure of cathode and anode. The ductile damage and damage evolution are used to describe the failure initiation and evolution for cathode and anode. The fracture strain/displacement at failure for cathode and anode are 0.14/0.09 mm and 0.45/0.8 mm, respectively. To improve computational stability, both surface-to-surface contact and general contact (explicit) algorithms are used.

4. Results and discussion

4.1. Simulation results and validation

4.1.1. Component modeling results and validation

The force-displacement response of cathode from simulation under through-thickness compression can well agree with the experiment result, and the Mises stress distribution in cross-section is homogeneous, indicating a reliable simulation result as shown in Fig. S5(a). As for anode, the model can accurately describe the gradual compaction process and the inflection point followed by the hardening stage (Fig. S5 (b)). Thanks to the constitutive model specified by the user subroutine VUMAT, the FE model can precisely describe its anisotropic mechanical behaviors, as well as the force-displacement in through-thickness compression or tension in various directions (i.e. MD, DD, and TD) shown in Fig. S5(c)–(f). The great consistency of simulation and experiment results demonstrates the validity of constitutive models for cathode, anode, and separator.

4.1.2. Stack modeling results and validation

Taking the validated constitutive stress-strain relationships of components as input material properties, we may obtain the stack modeling results. Compared with experiments, the stack model can well describe the mechanical force-displacement responses (i.e., force increasing stage followed by the drop stage), under both sphere indentation and cylinder compression, as shown in Fig. 5(a) and (b), respectively. The consistent comparison results demonstrate the validity of the stack model.

4.2. Short-circuit criteria based on separator deformation

Based on the validated models for components and anode-separator-cathode stack, the status parameters of the separator at ISC point can be extracted and analyzed. As mentioned above, the occurrence of ISC is attributed to the "failure" of the separator, either flattening or fracture. Herein from a mechanical point of view, two short-circuit criteria for both function failure and mechanical failure are established based on the mechanical deformation parameters of the separator from the stack model subjected to mechanical loading. These two criteria are strain-based, i.e., volumetric strain and equivalent strain.

The volumetric strain is expressed as follows:

$$\varepsilon_V = J_1 + J_2 + J_3 \tag{3}$$

where J_i $(i = 1, 2, 3)$ represents the invariants of strain tensor and can be expressed in terms of principal strains ε_i $(i = 1, 2, 3)$:

$$J_1 = \varepsilon_1 + \varepsilon_2 + \varepsilon_3 \tag{4}$$

$$J_2 = \varepsilon_1\varepsilon_2 + \varepsilon_2\varepsilon_3 + \varepsilon_3\varepsilon_1 \tag{5}$$

$$J_3 = \varepsilon_1\varepsilon_2\varepsilon_3 \tag{6}$$

Since quadratic and cubic terms are small compared with the first-order term and can be neglected, the reduced form of volumetric strain can be written as:

$$\varepsilon_V = J_1 = \varepsilon_1 + \varepsilon_2 + \varepsilon_3 \tag{7}$$

As to equivalent strain, the expression is:

$$\varepsilon_{eq} = \sqrt{\frac{1}{2}[(\varepsilon_1 - \varepsilon_2)^2 + (\varepsilon_2 - \varepsilon_3)^2 + (\varepsilon_3 - \varepsilon_1)^2]} \tag{8}$$

Note that strain ε used in this study is the logarithmic strain which

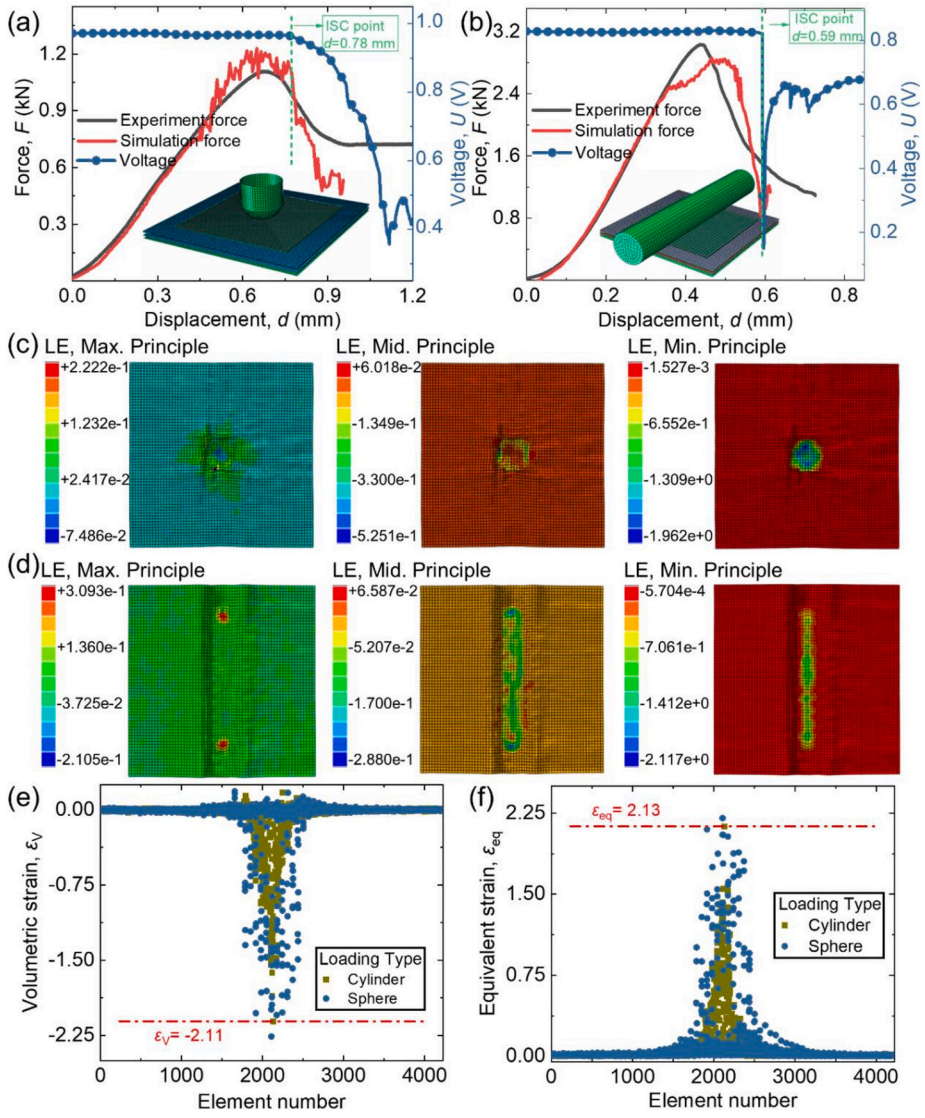

Fig. 5. Comparison of force-displacement responses in experiment and simulation for (a) sphere indentation and (b) cylinder compression. Contour plots of maximum, middle and minimum principal strains of the separator at short-circuit point for (c) sphere indentation and (d) cylinder compression. Two established short-circuit criteria based on the status of separator in sphere and cylinder loading models: (e) volumetric strain criterion and (f) equivalent strain criterion.

can be derived in terms of engineering strain e:

$$\varepsilon = \ln(1+e) \tag{9}$$

For both the volumetric strain and equivalent strain, all principal strains are taken into consideration. The loading displacements for sphere indentation and cylinder compression at ISC triggering points are 0.78 mm and 0.59 mm, respectively, which are selected from the earlist ISC points among all experiments. According to the contour plots of principal strains at ISC point for separator in the upper electrode pair shown in Fig. 5(c) and (d) for sphere indentation and cylinder compression respectively, strains only show in the loading zone and the strain in other areas is close to zero which exactly echos the actual loading conditions. The governing strain is minimum principal strain since its absolute value is much greater compared with maximum and middle principal strains, which indicates the primary loading type the separator mainly bears is compression. The most vulnerable zone is close to the loading center for sphere indentation, while it is near the two ends for cylinder compression since the sizes of anode and cathode are smaller than separator, which is similar to the actual possible loading situation in LIBs. More details about the evolutions of principal strains for separator under sphere indentation and cylinder compression can be found in Videos 1 to 6 in Supplementary Material.

The mesh convergence study has been conducted for the model, and different separator size less than 1 mm has little effect on the force-increasing stage. The element size selected for the separator is about 0.6 mm and there are 4225 elements in total for the upper separator. According to Eqs. (7) and (8), the volumetric strain and equivalent strain can be obtained for all separator elements. If we put all strain values at each element (represented by the element number) together as Fig. 5(e) and (f), there will be a prominent tip strain value point in each loading scenario. This tip point can serve as the safety boundary representing the threshold strain value, and once the strain reaches or exceeds this value, ISC is triggered. As such, we take the smaller one of the threshold strain value in these two loading scenarios to establish an ISC criterion, i.e.,

$$\varepsilon_V = -2.11 \tag{10}$$

$$\varepsilon_{eq} = 2.13 \tag{11}$$

4.3. Short-circuit criteria validation

To verify the validity of the proposed criteria, another loading con-

dition, i.e. a new type of loading, i.e., flat-headed indentation, is applied to the anode-separator-cathode stack. In this case, the vicinity of the flat head of the indentor is expected to create a stress concentration which makes the deformation status more complicated than round-headed indentation (both sphere indentation and cylinder compression). The diameter of the indentor is 12 mm. The force-displacement response of simulation well describes the force increasing stage followed by the force drop stage, compared with the experiment result, as shown in Fig. 6(a). The predicted loading displacement at the short-circuit point is 0.503 mm. The volumetric strain and equivalent strain of separator elements calculated in terms of principal strains are plotted in Fig. 6(b) and (c), respectively. According to the abovementioned methodology, the lines at $\varepsilon_V = -2.11$and $\varepsilon_{eq} = 2.13$ serve as the ISC triggering threshold values. We observe that the ISC is predicted to appear once the threshold values are reached and no ISC can be seen even if we take one time step back based upon the computation model. Therefore, the proposed criteria also work well upon flat-headed indentation. The criteria and development methodology are proven.

5. Conclusion

The ISC is directly related to the separator deformation status since ISC will be triggered once separator cannot block the electron transfer between cathode and anode. To fully investigate the quantitative relation between separator deformation and the onset of ISC, an anode-separator-cathode stack is designed and chosen for experiments. By using mechanical abusive loading as the ISC trigger, two characteristic short-circuit types were observed in anode-separator-cathode stack loading, i.e., rapid voltage drop under cylinder compression and gentle voltage drop under sphere indentation. The rapid voltage drop is due to the direct contact between cathode and anode as a result of separator fracture, while the gentle voltage drop is related to the flattening of the separator with the absence of its function to isolate electron transfer. The developed detailed numerical models of components (i.e., cathode, anode, and separator) and stack, considering the failure of anode and cathode and the anisotropy of separator, can well describe the mechanical responses of components under different loadings and stack

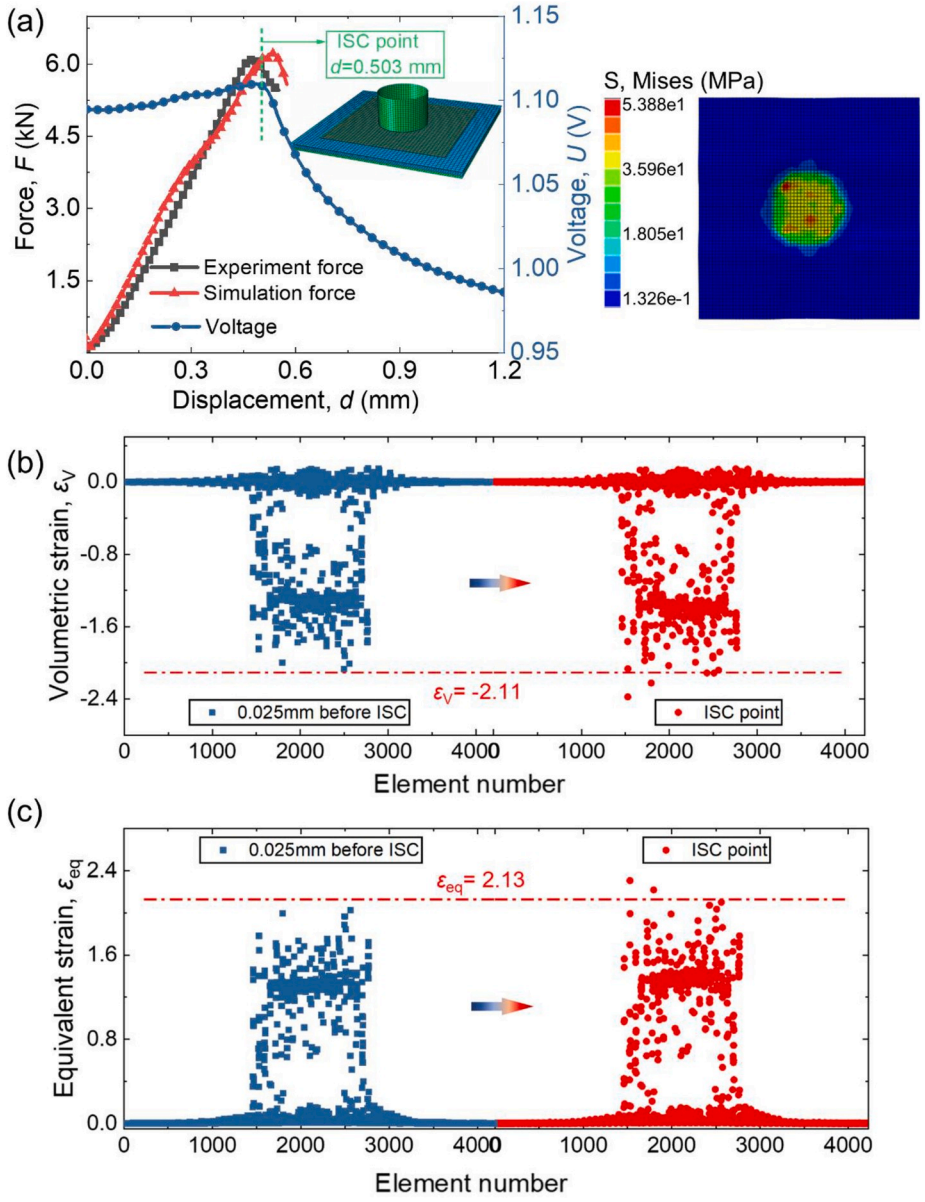

Fig. 6. Validation of proposed short-circuit criteria. (a) Comparison of force-displacement response in experiment and simulation for flat-headed indentation, and Mises stress for separator at short-circuit point. (b) Volumetric strain and (c) equivalent strain of separator at short-circuit point and 0.025 mm loading displacement before ISC served as validations of proposed criteria.

upon sphere and cylinder loading. Thanks to the FE model and computation, we established the generalized short-circuit criteria for the two representative failure modes based on the volumetric strain and equivalent strain of separator through sphere and cylinder loading conditions. The criteria proposed in this study is applicable for battery under various mechanical loadings, and further study should consider more loading scenarios, such as thermal loading. Guidance for the quantitative relationship between separator properties and the internal short circuit would benefit the next-generation separator designers in a more comprehensive way, which will be discussed elsewhere.

The developed methodology and proposed generalized criteria based on the deformation status of separator pave a solid fundamental towards a better understanding of the short-circuit triggering behavior of lithium-ion battery, and thus provide design guidance for the next-generation separator, as well as facilitating the monitoring, early detection, and evaluation of the ISC of batteries.

Author contribution

J. X. conceived the study and supervised the work. C. Y. and L. W. conducted the experiment and established the computational model. C. Y., S. Y. and J. X. analyzed the data. C. Y. and J. X. wrote the manuscript.

Declaration of competing interest

The authors declare that they have no known competing financial interests or personal relationships that could have appeared to influence the work reported in this paper.

CRediT authorship contribution statement

Chunhao Yuan: Writing - original draft, Investigation, Formal analysis. **Lubing Wang:** Data curation, Validation. **Sha Yin:** Validation, Funding acquisition. **Jun Xu:** Conceptualization, Methodology, Project administration, Supervision, Writing - review & editing.

Acknowledgment

L. W. and S. Y. would like to thank the financial support by The National Key Research and Development Program of China (2017YFB0103703) and The National Science Foundation of China (11872099).

Appendix A. Supplementary data

Supplementary data to this article can be found online at https://doi.org/10.1016/j.jpowsour.2020.228360.

References

[1] V. Etacheri, R. Marom, R. Elazari, G. Salitra, D. Aurbach, Energy Environ. Sci. 4 (2011) 3243–3262.
[2] B. Liu, Y. Jia, C. Yuan, L. Wang, X. Gao, S. Yin, J. Xu, Energy Storage Mater. 24 (2020) 85–112.
[3] V. Ruiz, A. Pfrang, A. Kriston, N. Omar, P. Van den Bossche, L. Boon-Brett, Renew. Sustain. Energy Rev. 81 (2018) 1427–1452.
[4] B. Liu, Y. Jia, J. Li, S. Yin, C. Yuan, Z. Hu, L. Wang, Y. Li, J. Xu, J. Mater. Chem. 6 (2018) 21475–21484.
[5] S. Abada, M. Petit, A. Lecocq, G. Marlair, V. Sauvant-Moynot, F. Huet, J. Power Sources 399 (2018) 264–273.
[6] Q. Wang, P. Ping, X. Zhao, G. Chu, J. Sun, C. Chen, J. Power Sources 208 (2012) 210–224.
[7] C. Yuan, X. Gao, H.K. Wong, B. Feng, J. Xu, J. Electrochem. Soc. 166 (2019) A1160–A1169.
[8] P. Bai, J. Guo, M. Wang, A. Kushima, L. Su, J. Li, F.R. Brushett, M.Z. Bazant, Joule 2 (2018) 2434–2449.
[9] S. Santhanagopalan, P. Ramadass, J. Zhang, J. Power Sources 194 (2009) 550–557.
[10] H. Wang, S. Simunovic, H. Maleki, J.N. Howard, J.A. Hallmark, J. Power Sources 306 (2016) 424–430.
[11] T. Yokoshima, D. Mukoyama, F. Maeda, T. Osaka, K. Takazawa, S. Egusa, S. Naoi, S. Ishikura, K. Yamamoto, J. Power Sources 393 (2018) 67–74.
[12] J. Xu, Y. Jia, B. Liu, H. Zhao, H. Yu, J. Li, S. Yin, Exp. Mech. 58 (2018) 633–643.
[13] B. Liu, S. Yin, J. Xu, Appl. Energy 183 (2016) 278–289.
[14] J. Ye, H. Chen, Q. Wang, P. Huang, J. Sun, S. Lo, Appl. Energy 182 (2016) 464–474.
[15] C.F. Lopez, J.A. Jeevarajan, P.P. Mukherjee, J. Electrochem. Soc. 162 (2015) A2163–A2173.
[16] A. Terella, F. De Giorgio, M. Rahmanipour, L. Malavolta, E. Paolasini, D. Fabiani, M.L. Focarete, C. Arbizzani, J. Power Sources 449 (2020) 227556.
[17] M.F. Lagadec, R. Zahn, V. Wood, Nat. Energy 4 (2018) 16–25.
[18] C.M. Costa, Y.H. Lee, J.H. Kim, S.Y. Lee, S. Lanceros-Mendez, Energy Storage Mater. 22 (2019) 346–375.
[19] H. Lee, M. Yanilmaz, O. Toprakci, K. Fu, X. Zhang, Energy Environ. Sci. 7 (2014) 3857–3886.
[20] P. Arora, Z.M. Zhang, Chem. Rev. 104 (2004) 4419–4462.
[21] J. Chen, Y. Yan, T. Sun, Y. Qi, X. Li, J. Electrochem. Soc. 161 (2014) A1241–A1246.
[22] S. Yan, J. Deng, C. Bae, X. Xiao, Polym. Test. 71 (2018) 65–71.
[23] J. Xu, L. Wang, J. Guan, S. Yin, Mater. Des. 95 (2016) 319–328.
[24] S. Kalnaus, Y. Wang, J.A. Turner, J. Power Sources 348 (2017) 255–263.
[25] J. Cannarella, X. Liu, C.Z. Leng, P.D. Sinko, G.Y. Gor, C.B. Arnold, J. Electrochem. Soc. 161 (2014) F3117–F3122.
[26] X. Zhang, E. Sahraei, K. Wang, J. Power Sources 327 (2016) 693–701.
[27] L. Ding, C. Zhang, T. Wu, F. Yang, Y. Cao, M. Xiang, J. Power Sources 451 (2020).
[28] S. Yan, J. Deng, C. Bae, Y. He, A. Asta, X. Xiao, Polym. Test. 72 (2018) 46–54.
[29] S. Kalnaus, Y. Wang, J. Li, A. Kumar, J.A. Turner, Extreme Mech. Lett. 20 (2018) 73–80.
[30] C. Peabody, C.B. Arnold, J. Power Sources 196 (2011) 8147–8153.
[31] J. Cannarella, C.B. Arnold, J. Power Sources 226 (2013) 149–155.
[32] G.Y. Gor, J. Cannarella, C.Z. Leng, A. Vishnyakov, C.B. Arnold, J. Power Sources 294 (2015) 167–172.
[33] S. Yan, X. Huang, X. Xiao, J. Power Sources 382 (2018) 13–21.
[34] A. Sheidaei, X. Xiao, X. Huang, J. Hitt, J. Power Sources 196 (2011) 8728–8734.
[35] W.Q. Hao, J.M. Xie, X. Zhang, P. Wang, F.H. Wang, Express Polym. Lett. 14 (2020) 206–219.
[36] H. Xu, C. Bae, J. Power Sources 430 (2019) 67–73.
[37] H. Xu, M. Zhu, J. Marcicki, X.G. Yang, J. Power Sources 345 (2017) 137–145.
[38] J. Zhu, X. Zhang, H. Luo, E. Sahraei, Appl. Energy 224 (2018) 251–266.
[39] X. Zhang, J. Zhu, E. Sahraei, RSC Adv. 7 (2017) 56099–56107.
[40] S. Kalnaus, A. Kumar, Y. Wang, J. Li, S. Simunovic, J.A. Turner, P. Gorney, J. Power Sources 378 (2018) 139–145.
[41] X. Zhang, E. Sahraei, K. Wang, Sci. Rep. 6 (2016) 32578.
[42] H. Wang, A. Kumar, S. Simunovic, S. Allu, S. Kalnaus, J.A. Turner, J.C. Helmers, E. T. Rules, C.S. Winchester, P. Gorney, J. Power Sources 341 (2017) 156–164.
[43] A. Sarkar, P. Shrotriya, A. Chandra, J. Power Sources 435 (2019) 226756.
[44] J. Chen, T. Sun, Y. Qi, X. Li, Ecs Electrochem. Lett. 3 (2014) A41–A44.
[45] H. Luo, Y. Xia, Q. Zhou, J. Power Sources 357 (2017) 61–70.
[46] G.D. Dean, W. Broughton. Polym. Test. 26 (2007) 1068–1081.
[47] J. Zhu, W. Li, T. Wierzbicki, Y. Xia, J. Harding, Int. J. Plast. 121 (2019) 293–311.
[48] L. Wang, S. Yin, J. Xu, J. Power Sources 413 (2019) 284–292.